International Journal of Research in Engineering and Science (IJRES)
ISSN (Online): 2320-9364, ISSN (Print): 2320-9356
www.ijres.org Volume 10 Issue 3 ǁ 2022 ǁ PP. 59-79

Room temperature strength, high temperature quasi-superplasticity, microstructural evolution and constitutive modeling in a superlight Mg-2.65Li-7.05Al-2.08Zn-0.15Y alloy

Furong Cao [a,b,c *], Siyuan Liu [a] , Renjie Liu [a], Jinrui Liang [a] , Huizhen Guo [a], Nanpan Guo [a]

[a] *School of Materials Science and Engineering, Northeastern University, Shenyang 110819, People's Republic of China*
[b] *Key Laboratory of Lightweight Structural Materials Liaoning Province, Northeastern University, Shenyang 110819, People's Republic of China*
[c] *State Key Laboratory of Rolling and Automation, Northeastern University, Shenyang 110819, People's Republic of China*
**Corresponding author: Furong Cao (F.R.Cao), E-mail: cfr-lff@163.com; caofr@smm.neu.edu.cn*

Abstract *To improve the strength at room temperature and ductility at high temperature, a novel α-Mg phase based multicomponent Mg-2.65Li-7.05Al-2.08Zn-0.15Y alloy difficult to roll has been successfully fabricated by decreasing-temperature multidirectional forging and hot rolling. The optical microstructural examination revealed that the average grain size of the processed alloy plate is 13.94 ± 1.0 μm. The ultimate tensile strength, 0.2% proof stress, and elongation of 295 MPa, 200 MPa, and 17.79%, respectively, were obtained at room temperature. The maximum quasi-superplasticity of 310% was demonstrated in this alloy at a temperature of 573 K and a strain rate of* 1.67×10^{-4} s^{-1}*. Flow stress curves showed that discontinuous dynamic recrystallization and continuous dynamic recrystallization occurred in this alloy at elevated temperatures and different strain rates in most cases, but the flow hardening phenomenon was discovered at a temperature of 633 K and strain rates of* 5×10^{-4} -1.67×10^{-4} s^{-1}*, resulting from the occurrence of grain coarsening. The established modified Zerilli-Armstrong constitutive model was incorporated into dislocation models to realize the estimation of the dislocation density and number of dislocations inside a grain under specific conditions. It was discovered that dozens of dislocations inside a fine grain formed by dynamic recrystallization favored intragranular dislocation glide and disfavored grain boundary sliding. A power-law constitutive equation was established, and the relationship between average grain size and Zener-Hollomon parameter was established in this alloy. It was found that at 573 K and* 1.67×10^{-4} s^{-1} *, the stress exponent was 3, and the experimental activation energy for deformation was 150.8 kJ/mol; the dislocation density was* 1.08×10^{14} m^{-2}*, and the number of dislocations inside a grain was 27. These results confirm that the rate-controlling deformation mechanism of this alloy under this condition is dislocation viscous glide creep controlled by lattice diffusion.*

Keywords *Magnesium; multidirectional forging; superplasticity; microstructure; mechanical property; constitutive model*

Date of Submission: 18-02-2022 Date of acceptance: 03-03-2022

I. Introduction

Mg-Li alloys, the lightest alloy with a density of 1.3-1.65 g cm^{-3}, have the potential for applications in spaceflight, military weapons, communication and electronic devices, and automobile sectors due to their extremely low density, high specific stiffness, high specific strength, good damping properties, and excellent electromagnetic shielding properties [1]. Thus, Mg-Li alloys recently have drawn much attention of researchers [2-11]. There are some reports available on single phase β-Li alloys [2, 3] and dual phase α-Mg+β-Li alloys [4-9]. Only a few reports have been reported in α-Mg based alloys [10-11]. Therefore, a novel α-Mg based Mg-3Li-7Al-2Zn-0.5Y alloy (designated as LAZY3720) is designed. The purpose of addition of 3 wt.% Li is to obtain α-Mg matrix according to binary Mg-Li phase diagram. The purpose of addition of 7 wt.% Al is to achieve solid solution strengthening and the second phase strengthening. The purpose of addition of 2 wt.% Zn is to achieve solid solution strengthening. The purpose of addition of 0.5 wt.% Y is to achieve grain refinement and the second phase strengthening. Due to insufficient slip systems of Mg and α-Mg based alloys, such alloys are difficult to deform at room temperature. Since high temperature deformation can activate non-basal slip systems of Mg and α-Mg based alloys, the deformability or ductility can be enhanced greatly. Hence, it is necessary to study on the high temperature deformation behavior and microstructure evolution in the LAZY3720 alloy. In addition, the room temperature properties are investigated.

Grain refinement through thermomechanical processing improves both strength and ductility. Multidirectional forging (MDF), one of the severe plastic deformation approaches, of magnesium alloys recently has captured the attention of extensive researchers [12, 13]. The microstructures and mechanical properties have been concentratedly investigated in LA143[12] and AZ80-F[13] alloys. However, except for our previous works on superplasticity of dual-phase Mg-10.2Li-2.1Al-2.23Zn-0.2Sr alloy [14] and microstructure and ambient mechanical properties in dual-phase Mg-6.4Li-3.6Zn-0.37Al-0.36Y alloy [15] processed by MDFR (multidirectional forging and rolling), no information is available about the study on the novel α-Mg based LAZY3720 alloy processed by MDF and hot rolling (HR). Thus, it is necessary to fabricate this alloy via MDF+HR to overcome the difficult-to-roll problem and investigate its high temperature microstructures and mechanical properties.

Superplasticity means the capability of materials in exhibiting larger elongation or excellent ductility, typically several hundred and occasionally several thousand. Langdon proposed [16] that superplasticity exhibits more than 400% elongation and strain rate sensitivity of 0.5, but quasi-superplasticity exhibits 200-300% (below 400%) elongation and strain rate sensitivity of 0.33. Some recent works on superplasticity of simple binary and trinary fine-grained or ultrafine-grained Mg-Li alloys are available reporting the experimental results of superplasticity in the range of 621.1-1400% [17-21]. However, the superplasticity of complex multicomponent Mg-Li alloy is rarely reported. Therefore, it is necessary to investigate the superplasticity behavior in complex multicomponent LAZY3720 alloy processed by MDF+HR.

Constitutive equation or model reflects the relationship of deformation temperature, strain rate, and strain of materials, and is a prerequisite for determination of the forming load and implementation of finite element simulation. The study on the constitutive model has a significant meaning and scientific value on the practical engineering process. The constitutive models include physically based constitutive equation, phenomenological equation, and artificial neural network model [22]. Recently, Arrhenius phenomenological equation [23-25], modified Johnson-Cook (mJC) equation [26], modified Zerili-Armstrong (mZA) equation [27], and physically based equation [28] have been reported in different magnesium alloys. According to our literature survey, the quantification of internal state variables such as grain size, dislocation density, and the number of dislocations has been neglected in recent years during the study of hot deformation behavior. Moreover, the establishment of constitutive equation relies on the flow stress curves obtained from different forming paths such as hot compression, hot tension, and hot torsion. In Mg-Li alloys, a majority of reports are available on the Arrhenius equation via hot compression [29-33], but the hot tension behavior is rarely reported [14, 15, 34]. Hot tensile deformation behavior in multicomponent LAZY3720 alloy remains unknown. Therefore, it is necessary to establish mZA constitutive equation and combine the mZA equation with internal state variables in LAZY3720 alloy. On the other hand, power-law constitutive equation has been used in superplasticity and creep and has its scientific value in elucidating the deformation mechanism at elevated temperature. However, aforementioned recent reports on superplasticity of binary and trinary Mg-Li alloys are concentrated on the experimental results [17-21] and are in lack of quantification of the power-law constitutive model and elucidation of the deformation mechanism at elevated temperature. Hence, it is essential to establish the power-law equation and reveal the high temperature deformation mechanism in multicomponent LAZY3720 alloy.

In this work, the investigated contents include several aspects. Firstly, a novel LAZY3720 alloy was fabricated by novel MDF+HR. Secondly, the microstructural evolution and flow stress at room and elevated temperatures were investigated. Thirdly, mZA constitutive equation considering dislocation variables was newly established, and a power-law equation was established in this alloy. Fourthly, the high temperature deformation mechanism and the significance of established equations were elucidated.

II. Experimental Material And Method

2.1. Material processing

Mg, Al, Zn, and Li blocks (purity more than 99.9%) and Mg-30Y master alloy were used as the raw materials to prepare the LAZY3720 alloy ingot. Raw materials were melted in an electric resistance furnace and cast in a water-circulated copper mold, as detailed in reference [35]. The analyzed chemical composition was 2.65 Li, 7.05 Al, 2.08 Zn, 0.15 Y, and balanced Mg (wt. %), and the actual alloy ingot of Mg-2.65Li-7.05Al-2.08Zn-0.15Y was obtained. The ingot size was 200 × 100 × 30 mm^3. The ingot was homogenized at 553 K for 20 h. After milling of the ingot surface, the milled ingot was cut into billets with dimensions of 40 (length) × 22 (width) ×30 (height) mm^3. Then the billets were formed by MDF on a hydraulic press of 3 kN maximum load. The schematic diagram of MDF process is shown in Fig. 1. The billet was compressed in A plane for the first pass, then the formed billet was turned 90 degrees and compressed in C plane for the second pass, then the compressed billet was turned 90 degrees and compressed in B plane for the third pass. This process was repeated until the required accumulative strain was attained. The MDF adopted the mode of decreased-temperature forging: 673 K for the 1st to 3rd pass, 623 K for the 4th to 6th pass, and 573 K for the 7th to 9th pass. The pass strain was 0.6. The MDF billets were hot rolled at 588 K to 12 mm on a two-high rolling mill. The HR reduction was 50%. Detailed rolling process was as follows: After holding at 588 K for 1 hour, the MDF billets were rolled from 24 mm to 20 mm for two passes with a pass reduction of 8.3%. The rolled plate after heating at 588 K for 15 min was rolled to 17 mm for three passes with a pass reduction of 4.3%. Then the rolling process was repeated for the latter six passes with a pass reduction of 4.3%, that is to say, the plate was rolled to 14 mm for three passes and to 12 mm for another three passes. After MDF and HR, the workpieces were water quenched to ambient temperature to reserve the microstructures at high temperatures.

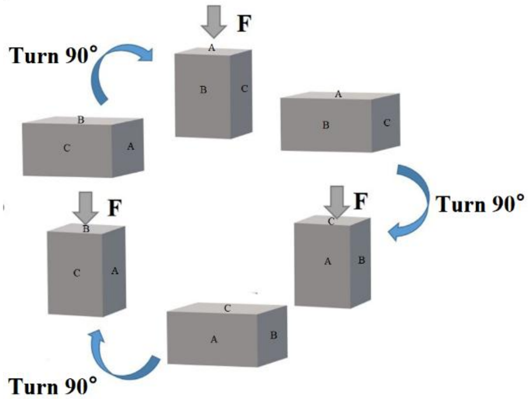

Fig. 1. Schematic diagram of multi-direction forging process. F denotes the forging pressing force and indicates the forging direction.

2.2. *Tensile tests at ambient and elevated temperatures*

Dog-bone shaped samples were machined on the rolled plate. The dimensions of the dog-bone shaped sample were 2 mm (thickness) ×10 mm (gauge length) × 6 mm (gauge width).The gauge direction was parallel to the rolling direction or longitudinal direction. Tensile tests were conducted on Shimidazu AG-X Plus universal tensile tester. The ambient tensile velocity is 3 mm per minute. After holding at 573 K for 15 min, high-temperature tensile tests were performed in a temperature range of 543−633 K over a strain rate range of $1.67\times10^{-2}-1.67\times10^{-4}$ s^{-1}.

2.3. *Microstructural characterization*

Samples for optical microscopy (OM) observation were prepared by conventional metallographic method. The samples were ground, polished, and etched in a 6 g picric acid +10 mL water + 50 mL absolute ethyl alcohol + 5 mL glacial acetic acid. The etching time was 30 s. The OM observation was performed on Olympus DSX500 optical microscope. The grain size was measured by Image-Pro Plus (IPP) software. A sample for EBSD (Electronic Backscattered Diffraction) characterization was prepared as follows: The gauge sample in a length of 8 mm was ground by 1000#、2000#、3000#and 5000# abrasive papers, mechanically polished, and further polished by 697 Ilion Ⅱ Argon lon Polishing Instrument equipped with liquid nitrogen cooling station produced by Gatan Company in the United States, and the ion beam energy is 0.1-8 KV. EBSD was detected by FIB-SEM of crossbeam 550 with resolution of 3 nm and acceleration voltage of 30 KV manufactured by Carl Zeiss management Co., Ltd. The misorientation angles between 0° and 2° were not considered in order to prevent noise in the EBSD maps.

III. Results

3.1. Initial microstructures and ambient mechanical properties of this alloy before high temperature tensile deformation

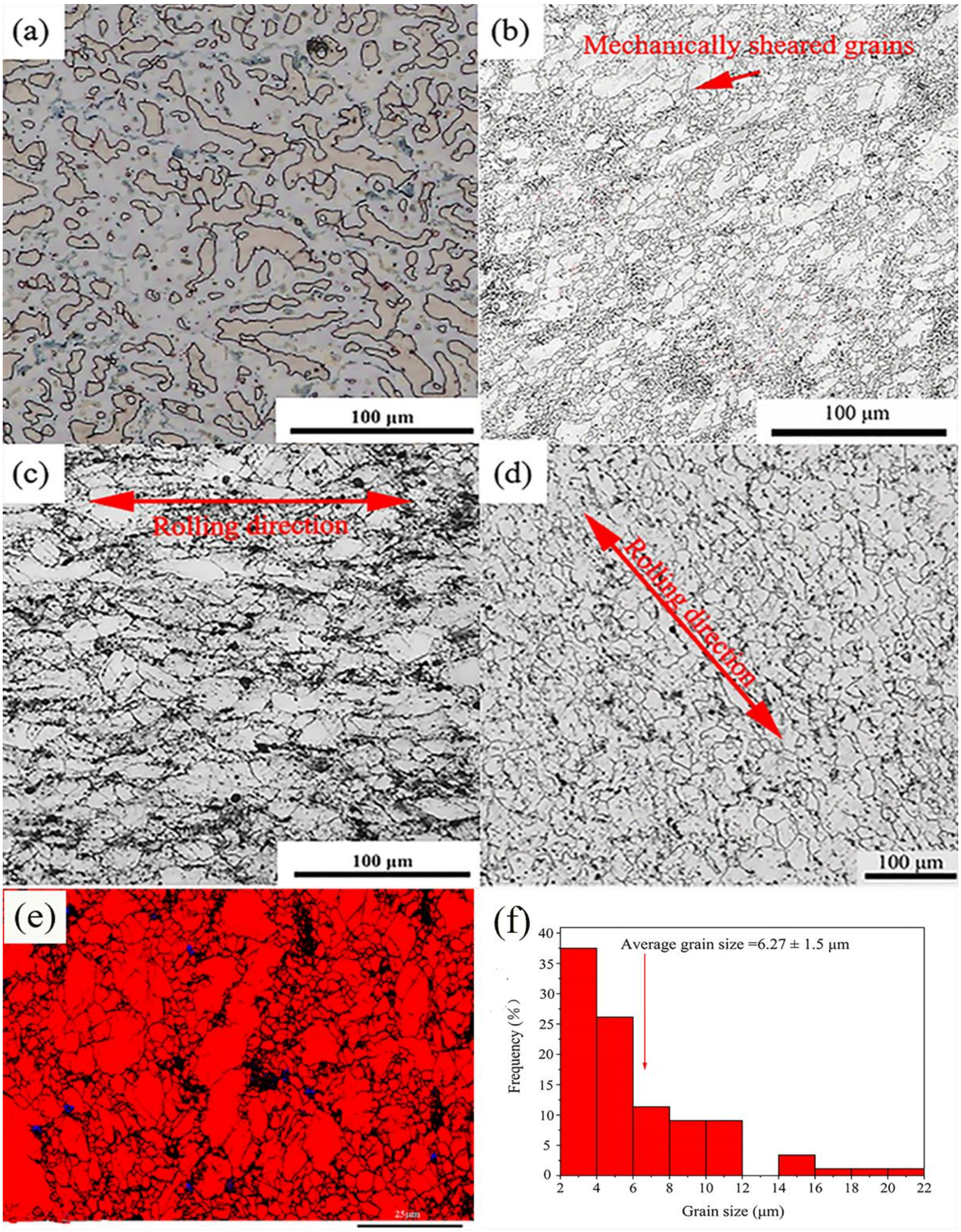

Fig. 2. OM microstructures of LAZY3720 alloy: (a) As-cast, (b) MDF, 6th pass, 623 K, (c) MDF+HR at a temperature of 588 K and a reduction of 50%, (d) annealed at 623 K for 1 h,(e) EBSD analysis of different types of grains in the alloy; blue and red color represent recrystallized and deformed grains, and (f) grain size distribution.

Fig. 2 presents the OM microstructures of LAZY3720 alloy after MDF+HR at a temperature of 588 K and a reduction of 50%. As shown in Fig. 2(a), grains in irregular shapes exist due to the rapid cooling of water-cooled copper mold. As shown in Fig. 2(b), after 6-pass MDF at a temperature of 623 K, the mechanically sheared grains and dynamically recrystallized (DRXed) grains appear because of the action of internal shear stress transformed from the compression stress in the vertical direction. The average grain size is 6.41 ± 1.0 μm.

The microstructure is a heterogeneous or non-uniform microstructure. As shown in Fig. 2(c), grains are in the elongated state. Grain aspect ratio (GAR) is defined as the ratio of horizontal grain size to vertical grain size. GAR value is only 1.65. The average grain size is 13.94 ± 1.0 μm. Compared to other Mg-Li alloys such as single phase β-Li and dual-phase α-Mg +β-Li alloys, the present alloy is difficult to be rolled because of high Al content (7.05 wt.%) and α-Mg hexagonal close-packed (HCP) structure. Intermediate annealing heated at 588 K for 15 min has to be added between rolling passes. Thus, grain coarsening following dynamic recrystallization (DRX) occurs in the MDF+HR microstructures. Even so, the MDF+HR microstructure still is a bimodal microstructure in which coarse grains account for a majority and fine grains account for a minority. As shown in Fig. 2(d), equiaxed grains exist due to static recrystallization. The average grain size is 16.5 ± 1.3 μm. This annealed microstructure provides a prerequisite for study on the high-temperature behavior. As shown in Fig. 2(e), EBSD analysis of 6-pass MDF sample in Fig 2(b) reveals that red deformed grains account for a majority, but blue recrystallized grains account for a minority. A small number of black grains cannot be identified by available EBSD technique. Hence, 6-pass MDF is a non-uniform deformed microstructure. As shown in Fig. 2(f), the average grain size is 6.27 ± 1.5 μm.

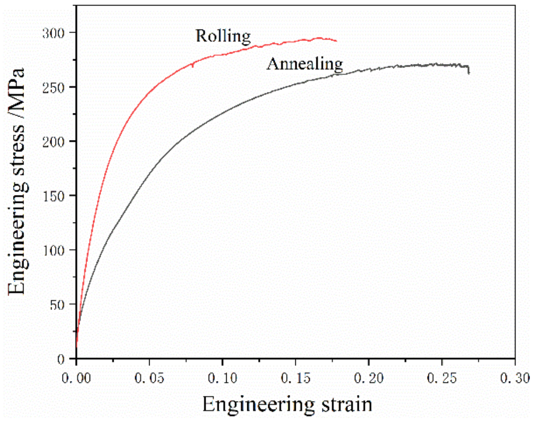

Fig. 3. Engineering stress-strain curves of MDF+HR and as-annealed specimens of LAZY3720 alloy.

Fig. 3 shows the stress-strain curves of MDF+HR and as-annealed specimens of LAZY3720 alloy. The ultimate tensile strength and 0.2% proof stress of MDF+HR alloy are 295 and 200 MPa, respectively, while the ultimate tensile strength of the as-annealed alloy is 271 MPa. The elongation of MDF+HR alloy is 17.79% while the elongation of the as-annealed alloy is 26.83%. High Al content (7.05%) and α-Mg phase matrix are favorable for the excellent mechanical properties. Annealing leads to the decrease in ultimate tensile strength and increase in elongation in the present alloy. Serrated flow or Portevin-Le Chatelier (PLC) effect can be seen in Fig. 3. PLC effect is observed in this alloy and is caused by the pinning and depinning of Cottrell's atmosphere or the interaction between dislocations and solute Li, Al, and Zn.

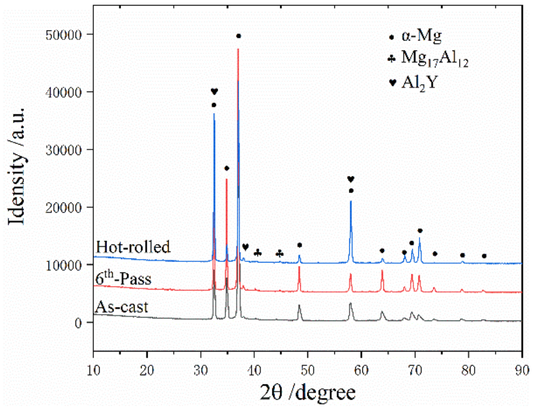

Fig. 4. XRD patterns of LAZY3720 alloy in different states.

Fig. 4 shows the XRD patterns of LAZY3720 alloy in different states. The present alloy consists of α-Mg solid solution and $Mg_{17}Al_{12}$, Al_2Y intermetallic compounds. Zn is dissolved in the matrix. These compounds and solutionized Zn contribute to the enhancement of mechanical properties.

3.2. Microstructures of this alloy after high temperature tensile deformation

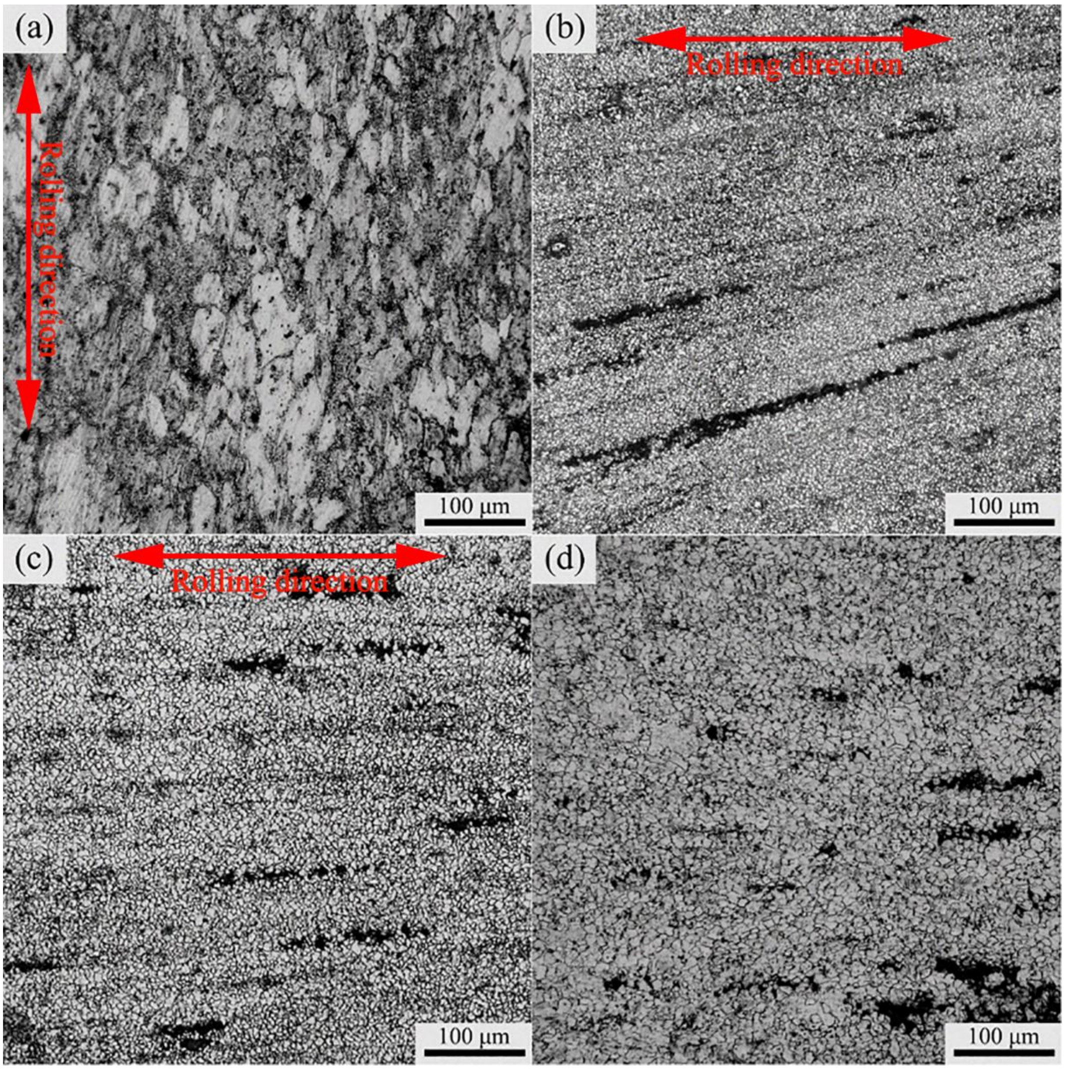

Fig. 5. Microstructures of gauge section in LAZY3720 alloy at a deformation temperature of 573 K with different strain rates, grain sizes, and elongations: (a)1.67×10^{-2} s^{-1}, *d*=15.5 ± 1.5 μm, δ=75%; (b)1.67×10^{-3} s^{-1}, *d* =3.3 ± 0.8 μm, δ=130%; (c)5×10^{-4} s^{-1}, *d*=4.2 ± 1.1 μm, δ=170%; (d)1.67×10^{-4} s^{-1}, *d*=6.2 ± 1.2 μm, δ=310%.

Fig. 5 presents the microstructures of gauge section in LAZY3720 alloy at a deformation temperature of 573 K with different strain rates. As shown in Fig. 5(a), at a strain rate of 1.67×10^{-2} s^{-1}, coarse grains exist with an average grain size of 15.5 ± 1.5 μm. Compared to the average grain size of 16.5 ± 1.3 μm in Fig. 2(d), DRX is slightly initiated according to the difference between the average grain sizes because the deformation time is very short at high strain rate though pre-heating lasts 15 min before tension. As shown in Fig. 5(b) and (c), compared to the average grain size of 15.5 ± 1.5 μm in Fig. 5(a), the average grain sizes were 3.3 ± 0.8 and 4.2 ± 1.1 μm , respectively, at strain rates of 1.67×10^{-3} and 5×10^{-4} s^{-1}. Thus, grains are well refined to fine-grained scale due to the occurrence of DRX, but the fine grains align along the rolling direction, indicative of the occurrence of incomplete DRX. As shown in Fig. 5(d), at a strain rate of 1.67×10^{-4} s^{-1}, the deformation time is prolonged, and sufficient DRX takes place. As a result, the maximum elongation of 310% is achieved at a fine grain size of 6.2 ± 1.2 μm.

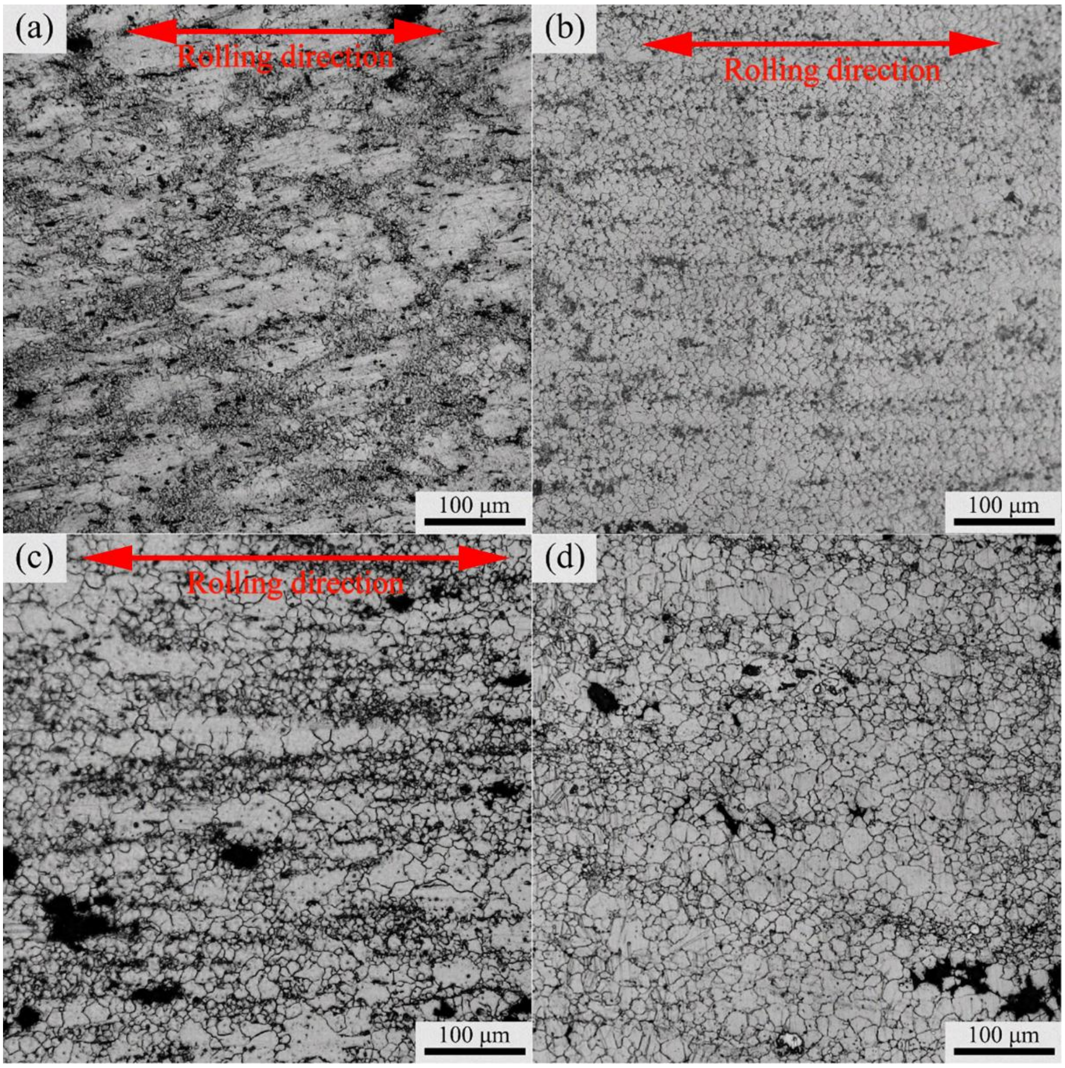

Fig. 6. Microstructures of gauge section in LAZY3720 alloy at a deformation temperature of 603 K with different strain rates, grain sizes, and elongations:(a)1.67×10^{-2} s^{-1}, d=12.6 ± 1.8 μm, δ=100%; (b)1.67×10^{-3} s^{-1}, d=6.3 ± 0.9 μm, δ=280%; (c)5×10^{-4} s^{-1}, d=7.6 ± 1.4 μm, δ=170%; (d)1.67×10^{-4} s^{-1}, d=7.9 ± 1.7 μm, δ=250%.

Fig. 6 presents the microstructures of gauge section in LAZY3720 alloy at a deformation temperature of 603 K with different strain rates. As shown in Fig. 6(a), at a strain rate of 1.67×10^{-2} s^{-1}, partial DRX or incomplete DRX occurs due to short deformation time. Coarse grains are surrounded by fine grains. As shown in Fig. 6(b), at a strain rate of 1.67×10^{-3} s^{-1}, partial DRX proceeds further, and fine-grained microstructure with horizontal rolling trace is formed. Thus, 280% elongation is obtained in this case. As shown in Fig. 6(c), at a strain rate of 5×10^{-4} s^{-1}, DRX develops further, and connected equiaxed fine grains with horizontal rolling traces are clearly visible. Some of extremely small grains are around the big grains, which proves the occurrence of discontinuous DRX. Also, in individual banded grain, separate grains are formed by continuous DRX due to tensile deformation. As shown in Fig. 6(d), at a strain rate of 1.67×10^{-4} s^{-1}, nearly full DRX occurs, equiaxed fine grains with high angle grain boundaries are visible, and the distribution of equiaxed fine grains is homogeneous. In a word, with the decrease in strain rate, the microstructure develops from incomplete DRX to nearly full DRX. Nearly full DRX or complete DRX predominates at the temperature of 603 K and strain rate of 1.67×10^{-4} s^{-1}.

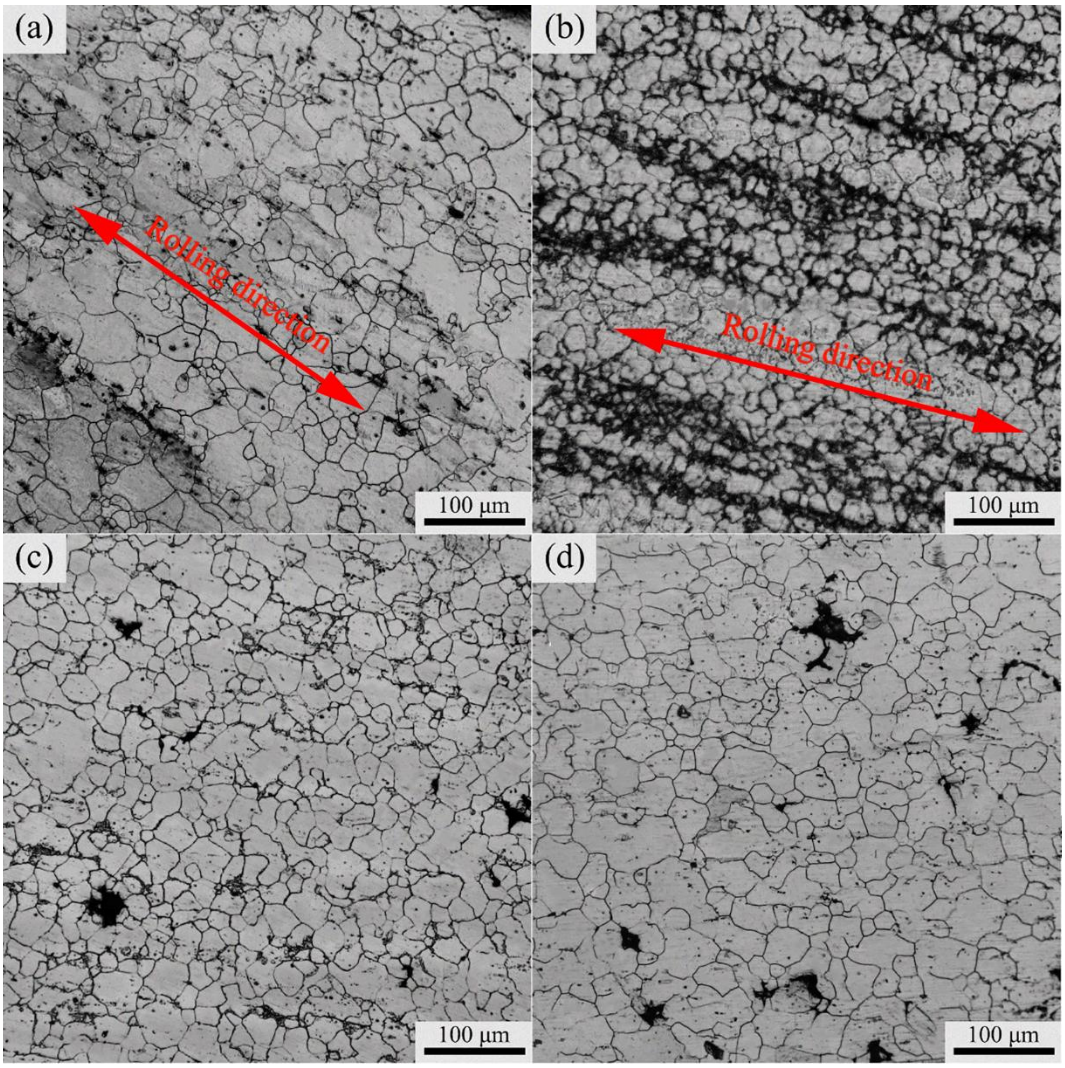

Fig. 7. Microstructures of gauge section in LAZY3720 alloy at a deformation temperature of 633 K with different strain rates, grain sizes, and elongations: (a)1.67×10^{-2} s^{-1}, d=16.8 ± 2.1 μm, δ=125%; (b)1.67×10^{-3} s^{-1}, d=17.3 ± 1.4 μm, δ=220%; (c)5×10^{-4} s^{-1}, d=17.8 ± 2.7 μm, δ=210%; (d)1.67×10^{-4} s^{-1}, d=23.4 ± 2.4 μm, δ=140%.

Fig. 7 presents the microstructures of gauge section in LAZY3720 alloy at a deformation temperature of 633 K with different strain rates. DRX and grain coarsening occur simultaneously at this temperature. As shown in Fig.7 (a) and (b), DRX occurs in the microstructures, but the connected equiaxed grains aligning along the rolling direction are visible. The degree of DRX is still partial or incomplete, and the distribution of grains is not homogeneous. Slight grain coarsening occurs. However, as shown in Fig.7 (c) and (d), full DRX and grain coarsening occur due to long-time deformation at elevated temperature. Fully equiaxed grains are clearly visible. Grain distribution becomes more homogeneous.

3.3. Stress-strain curves of this alloy at tensile temperatures

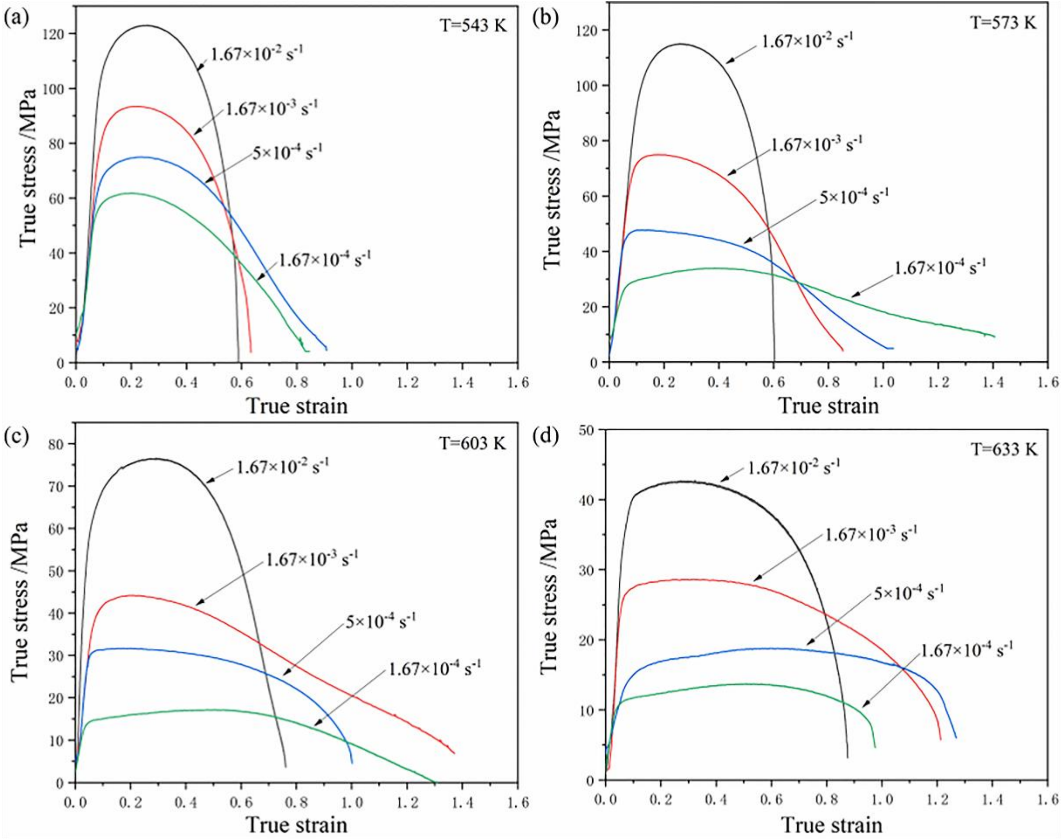

Fig. 8. True stress versus strain curves of LAZY3720 alloy at the same deformation temperatures with different strain rates: (a) 543 K; (b) 573 K; (c) 603 K; (d) 633 K.

Fig. 8 shows the true stress versus strain curves of LAZY3720 alloy at the same deformation temperatures with different strain rates. For a single stress-strain curve, the flow stress rises with increasing the strain, a short transitional stage of decreasing strain hardening rate appears until the peak stress. At the peak stress, the softening and hardening achieve a balance. After the peak stress, the flow stress decreases with increasing the strain, and usually flow softening occurs. For different stress-strain curves, the flow stress decreases with the increase in temperature and/or decrease in strain rate. Due to rapid atomic diffusion and decrease in dislocation density, the thermal activation process promotes the reduction of flow stress with the increase in temperature and/or decrease in strain rate. As shown in Fig. 8(a)(b)(c), after the peak stress, the flow stress decreases with increasing strain, indicative of the occurrence of DRX and flow softening. As shown in Fig. 8(d), the flow stress decreases with increasing strain at strain rates of 1.67×10^{-2} -1.67×10^{-3} s^{-1}, indicative of the occurrence of DRX and flow softening, but the flow stress increases with increasing the strain at strain rates of 5×10^{-4} -1.67×10^{-4} s^{-1}, indicative of the occurrence of grain coarsening and flow hardening. This reveals that DRX and grain coarsening occur at 633 K with different strain rates.

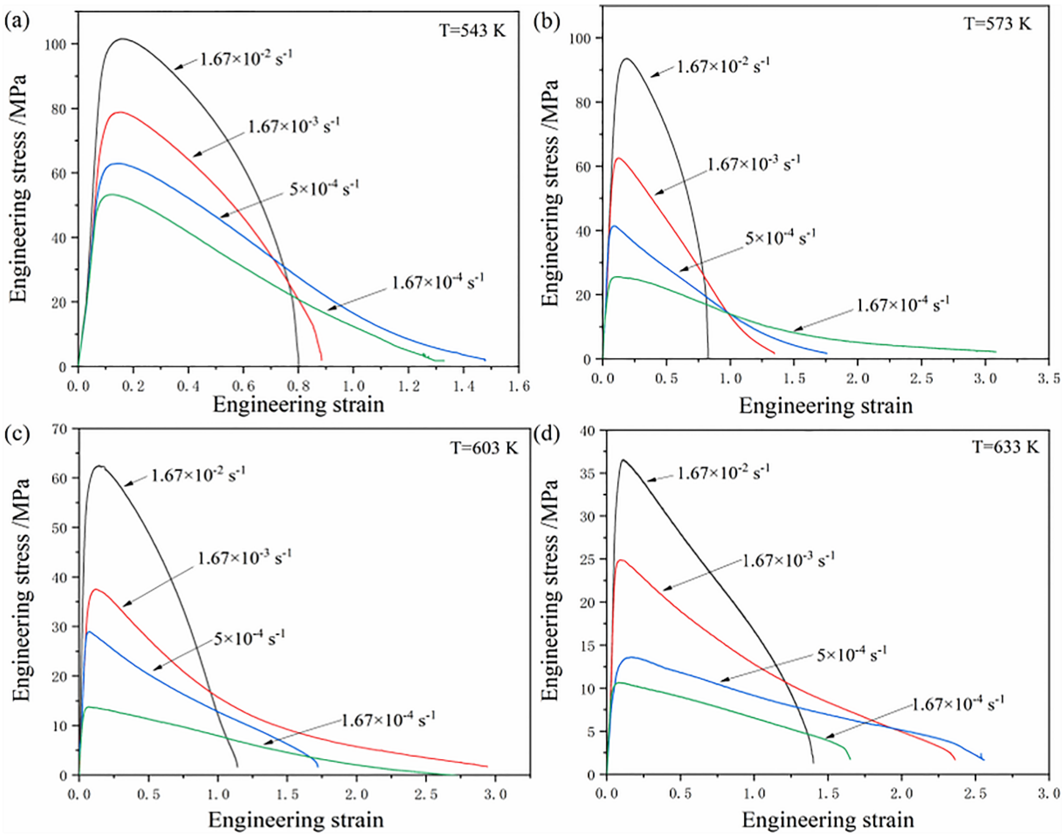

Fig.9. Engineering stress versus strain curves of LAZY3720 alloy at the same deformation temperatures with different strain rates: (a) 543 K; (b) 573 K; (c) 603 K; (d) 633 K.

Fig. 9 presents the engineering stress versus strain curves of LAZY3720 alloy at the same deformation temperatures with different strain rates. The elongations are in the range of 70-310%. As shown in Fig. 9(b), the maximum elongation to failure of 310% was obtained at 573 K and 1.67×10^{-4} s^{-1}. As shown in Fig. 9(c), the secondary elongation to failure of 280% was obtained at 603 K and 1.67×10^{-3} s^{-1}.

3.4. Constitutive modeling

3.4.1. Modified Zerilli-Armstrong constitutive equation

Modified Zerilli-Armstrong (mZA) constitutive equation is given by the following form [36]:

$$\sigma = (C_1 + C_2\varepsilon^n)\exp\left[-(C_3 + C_4\varepsilon)(T - T_{\mathrm{ref}}) + (C_5 + C_6(T - T_{\mathrm{ref}}))\ln(\dot{\varepsilon}/\dot{\varepsilon}_0)\right] \quad (1)$$

where C_1, C_2, C_3, C_4, C_5, C_6 , and n are material constants. These material constants need to be solved by means of experimental flow stress data. C_1 is the yield stress (50.07 MPa) of flow stress curves under referred strain rate and referred deformation temperature. Let referred strain rate $\dot{\varepsilon}_0$ be 1.67×10^{-4} s^{-1}, and let referred deformation temperature T_{ref} be 543 K. σ is the true stress, ε is the true strain, and $\dot{\varepsilon}$ is the strain rate.

When the strain rate is equal to the referred strain rate, Eq. (1) is converted to the following form:

$$\sigma = (C_1 + C_2\varepsilon^n)\exp\left[-(C_3 + C_4\varepsilon)(T - T_{\mathrm{ref}})\right] \quad (2)$$

Take logarithm, Eq. (2) becomes

$$\ln\sigma = \ln(C_1 + C_2\varepsilon^n) - (C_3 + C_4\varepsilon)(T - T_{\mathrm{ref}}) \quad (3)$$

Substitution of the flow stresses at referred strain rate into Eq. (3) and fitting linearly, $\ln\sigma - (T - T_{\mathrm{ref}})$ curves can be obtained, as shown in Fig. 10. $-(C_3 + C_4\varepsilon)$ and $\ln(C_1 + C_2\varepsilon^n)$ can be obtained according to the slope S_1 and intercept I_1.

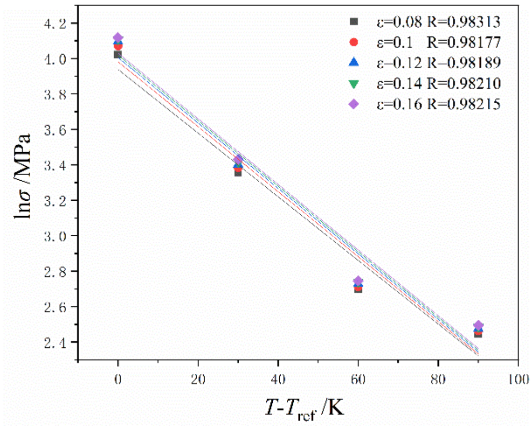

Fig. 10. Linear fitting curve of $\ln\sigma$ versus $T-T_{\text{ref}}$.

Thus, the following relation can be obtained:

$$\ln(\exp I_1 - C_1) = \ln C_2 + n\ln\varepsilon \qquad (4)$$

In like manner, $\ln(\exp I_1 - C_1)$ and $\ln\varepsilon$ are fitted linearly, one gets Fig. 11. In the same way, n (=6.05476) and C_2 (=2.20034 MPa) are obtained according to the slope and intercept of this curve.

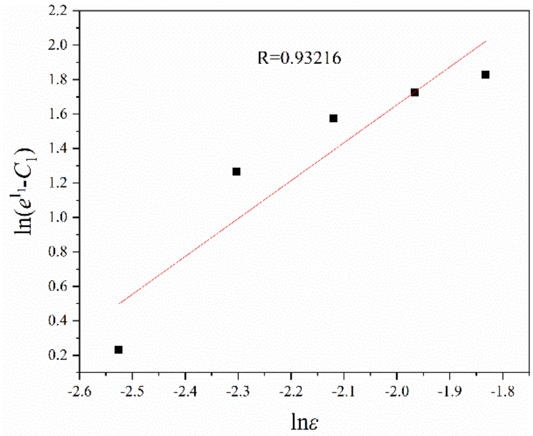

Fig. 11. Linear fitting curve of $\ln(\exp I_1 - C_1)$ versus $\ln\varepsilon$.

Based on what has been described above, the following relation exists.

$$S_1 = -(C_3 + C_4\varepsilon) \qquad (5)$$

S_1 and ε are fitted linearly, as shown in Fig. 12. In the same way, C_3 (=0.01758) and C_4 (=0.00635) are obtained according to the intercept and slope of this curve.

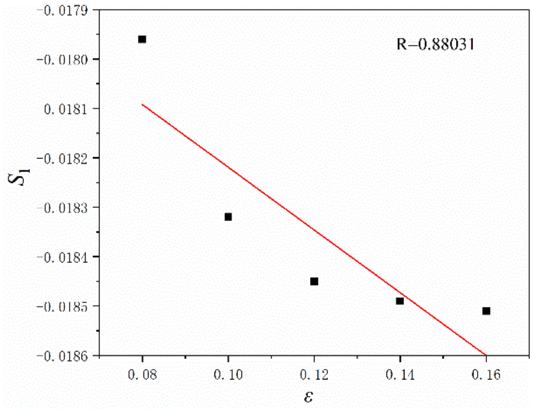

Fig. 12. Linear fitting curve of S_1 versus ε.

Take logarithm on both sides of Eq. (1), one gets

$$\ln\sigma = \ln(C_1 + C_2\varepsilon^n) - (C_3 + C_4\varepsilon)(T - T_{\text{ref}}) + [C_5 + C_6(T - T_{\text{ref}})]\ln(\dot{\varepsilon}/\dot{\varepsilon}_0) \quad (6)$$

According to Eq. (6), $\ln\sigma$ and $\ln(\dot{\varepsilon}/\dot{\varepsilon}_0)$ are fitted linearly, as shown in Fig. 13.

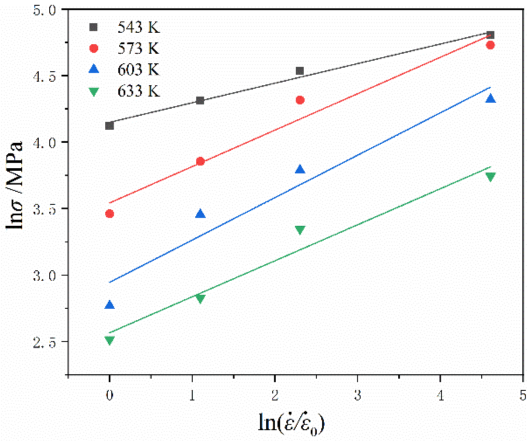

Fig. 13. Linear fitting curve of $\ln\sigma$ versus $\ln(\dot{\varepsilon}/\dot{\varepsilon}_0)$.

Let the slope of Fig. 13 be S_2, one gets

$$S_2 = C_5 + C_6(T - T_{\text{ref}}) \qquad (7)$$

Then S_2 and $(T - T_{\text{ref}})$ are fitted linearly, one gets Fig. 14. In the same way, C_5 (=0.1903) and C_6 (=0.00139) are obtained according to the intercept and slope of this curve.

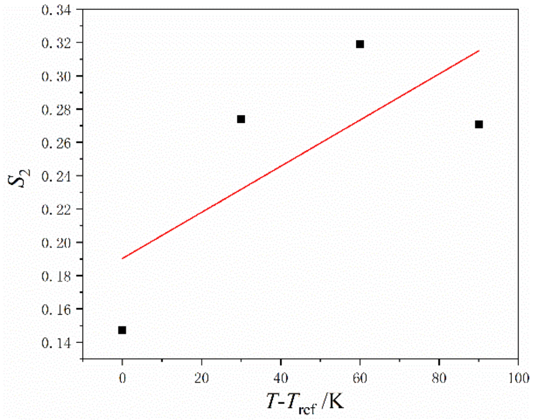

Fig. 14. Linear fitting curve of S_2 versus $T - T_{\text{ref}}$.

Substitution of aforementioned C_1, C_2,C_3,C_4, C_5, C_6, and n values into Eq. (1), the mZA constitutive equation is obtained as follows:

$$\sigma = (50.07 + 2.20034\varepsilon^{6.05476})\mathrm{e}^{-(0.01758+0.00635\varepsilon)(T-T_{\text{ref}})+[0.1903+0.00139(T-T_{\text{ref}})]\ln\left(\frac{\dot{\varepsilon}}{\dot{\varepsilon}_0}\right)}$$

$$= f(T, \dot{\varepsilon}, \varepsilon) \qquad (8)$$

Eq. (8) reflects quantitatively the relationship between flow stress and deformation condition such as temperature, strain rate, and strain in hot tensile LAZY3720 alloy.

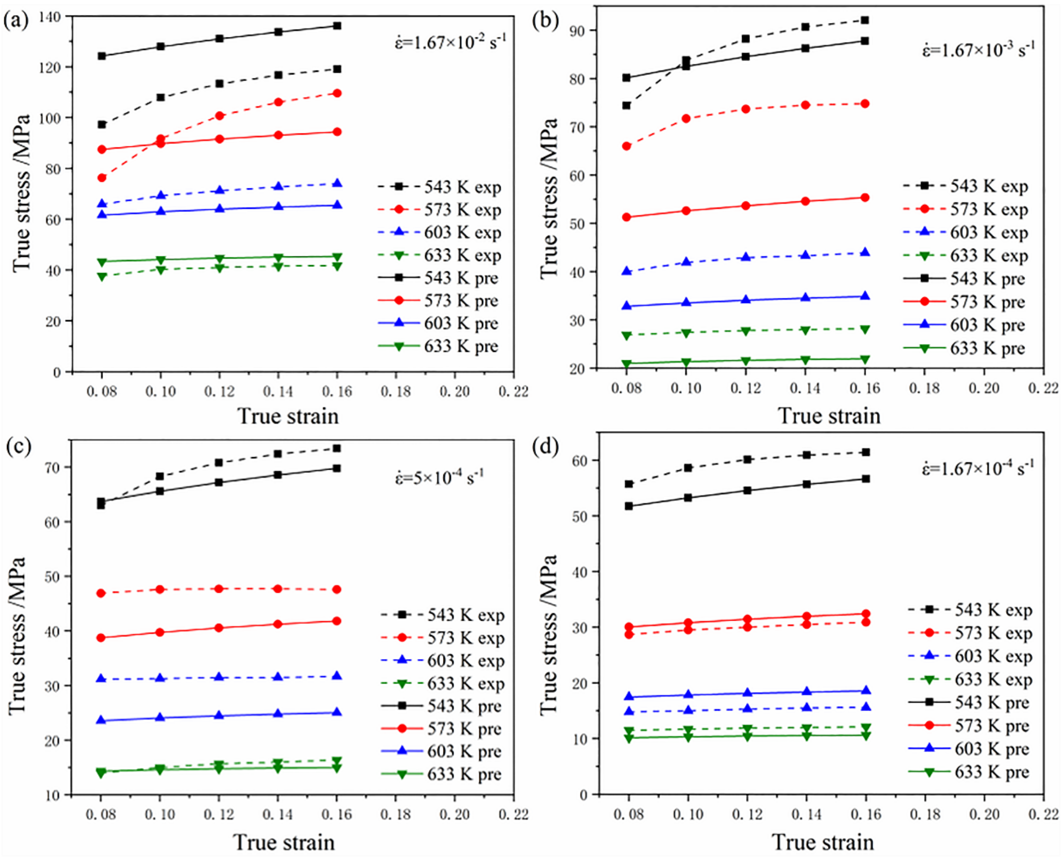

Fig. 15. Comparison between experimental and predicted flow stress values by the modified Zerilli-Armstrong model at different temperatures and different strain rates: (a) 1.67×10^{-2} s^{-1}; (b)1.67×10^{-3} s^{-1}; (c)5×10^{-4} s^{-1}; (d)1.67×10^{-4} s^{-1}. Here, exp denotes experiment stress and pre denotes prediction stress.

Fig. 15 shows the comparison between experimental and predicted flow stresses by the mZA model at different temperatures and different strain rates. As shown in Fig. 15(b) and (c), the error between experimental stress and predicted stress is relatively large, and the predictive effect is non-ideal. The absolute average relative error is 13.2%. However, as shown in Fig. 15(a) and (d), the predictive effect is ideal, especially, the predictive effect is the best at the temperatures of 603-633 K and a strain rate of 1.67×10^{-4} s^{-1}. More accurate mZA model needs to be established in the future.

The dislocation density and the number of dislocations inside a grain can be expressed as the following [37]

$$\rho=C(Gb)^{-2}\sigma^{2} \qquad (10)$$

$$N=1.81(1-\nu)[d/(Gb)]\,\sigma \qquad (11)$$

where ρ is the dislocation density, C is the dimensionless constant, G is the shear modulus, b is the magnitude of Burges vector, N is the number of dislocations inside a grain, ν is Poisson's ratio, and d is the linear intercept grain size.

Substitution of Eq. (8) into Eqs. (10) and (11) gives

$$\rho=C(Gb)^{-2}\,f(T,\dot{\varepsilon},\varepsilon)^{2} \qquad (12)$$

$$N=1.81(1-\nu)[d/(Gb)]\;f(T,\dot{\varepsilon},\varepsilon) \qquad (13)$$

Eqs. (12) and (13) are the constitutive equations containing dislocation density and number of dislocations, respectively. This indicates that dislocation variables under different deformation conditions, such as T,$\dot{\varepsilon}$, and ε, can be characterized based on the established mZA constitutive equation.

G for Mg is given by [38]

$$G\ (MPa)=1.66\times10^{4}[1-0.49(T-300)/943] \qquad (14)$$

Estimation is made for a specific deformation condition of true strain of 0.14 (elongation of 15%). T=573 K, $\dot{\varepsilon}$=1.67×10^{-4} s^{-1}, C=10[39], G=14245.19 MPa, b=3.21×10^{-10} m [40], ν=0.28 [40], d=1.65×10^{-5} m (Fig. 2(d)), and $f(T,\dot{\varepsilon},\varepsilon)$=28.66 MPa. Substitution of these data into Eqs. (12) and (13) give ρ=3.90×10^{14} m^{-2} and N=135. This result reveals that significant dislocation activity occurs in this alloy, and dislocation glide occurs under this condition. Moreover, estimation is extended to a specific deformation condition of 310% elongation (true strain of 1.41). T=573 K, $\dot{\varepsilon}$=1.67×10^{-4} s^{-1}, d=6.2×10^{-6} m (Fig. 5(d)), and σ=15 MPa (Fig. 8(b)). Substitution of these data into Eqs. (10) and (11) give $\rho=1.08\times10^{14}$ m^{-2} and N=27. This result reveals that remarkable dislocation activity occurs in this alloy, and dislocation glide creep governs the rate-controlling mechanism under this condition. The estimated results also reveal that the dislocation density and number of dislocations decrease sharply with increasing the strain, and hence flow softening occurs due to the occurrence of DRX under this condition.

3.4.2. Power-law constitutive equation

This section will establish high temperature power-law constitutive equation of LAZY3720 alloy via determination of several key characteristic exponents such as stress exponent, grain size exponent, and activation energy for deformation.

High temperature power-law constitutive equation is generally given by [41]

$$\dot{\varepsilon} = \frac{AD_0Gb}{kT}\left(\frac{b}{d}\right)^p\left(\frac{\sigma-\sigma_0}{G}\right)^n \exp\left(-\frac{Q}{RT}\right) \qquad (15)$$

where $\dot{\varepsilon}$ is the steady-state deformation rate, A is a dimensionless constant, G is the shear modulus, b is the magnitude of Burgers vector, p is the grain size exponent, σ is the applied stress, n is the stress exponent ($1/m$, m-strain rate sensitivity exponent or m-value), D_0 is the frequency factor for diffusion, Q is the activation energy for deformation, k is Boltzmann's constant, T is the absolute temperature, d is the grain size, and R is the universal gas constant.

(1) Threshold stress σ_0 and stress exponent n

Stress exponent, n, is related to threshold stress, σ_0. Threshold stress is the onset stress to initiate the plastic flow. True stress at a true strain of 0.2 is chosen from the flow stress curves. Then, $\sigma-\dot{\varepsilon}^{1/2}, \sigma-\dot{\varepsilon}^{1/3}, \sigma-\dot{\varepsilon}^{1/4}$, and $\sigma-\dot{\varepsilon}^{1/5}$ curves are fitted linearly. The intercepts of the linear curve are the threshold stresses, respectively, when n are 2, 3, 4, and 5. When σ_0 value is positive and the fitting quality or correlation coefficient is the best, corresponding n value is the optimal value. Fig. 16 presents the linear fitting curves of $\sigma-\dot{\varepsilon}^{1/2}, \sigma-\dot{\varepsilon}^{1/3}, \sigma-\dot{\varepsilon}^{1/4}$, and $\sigma-\dot{\varepsilon}^{1/5}$, respectively.

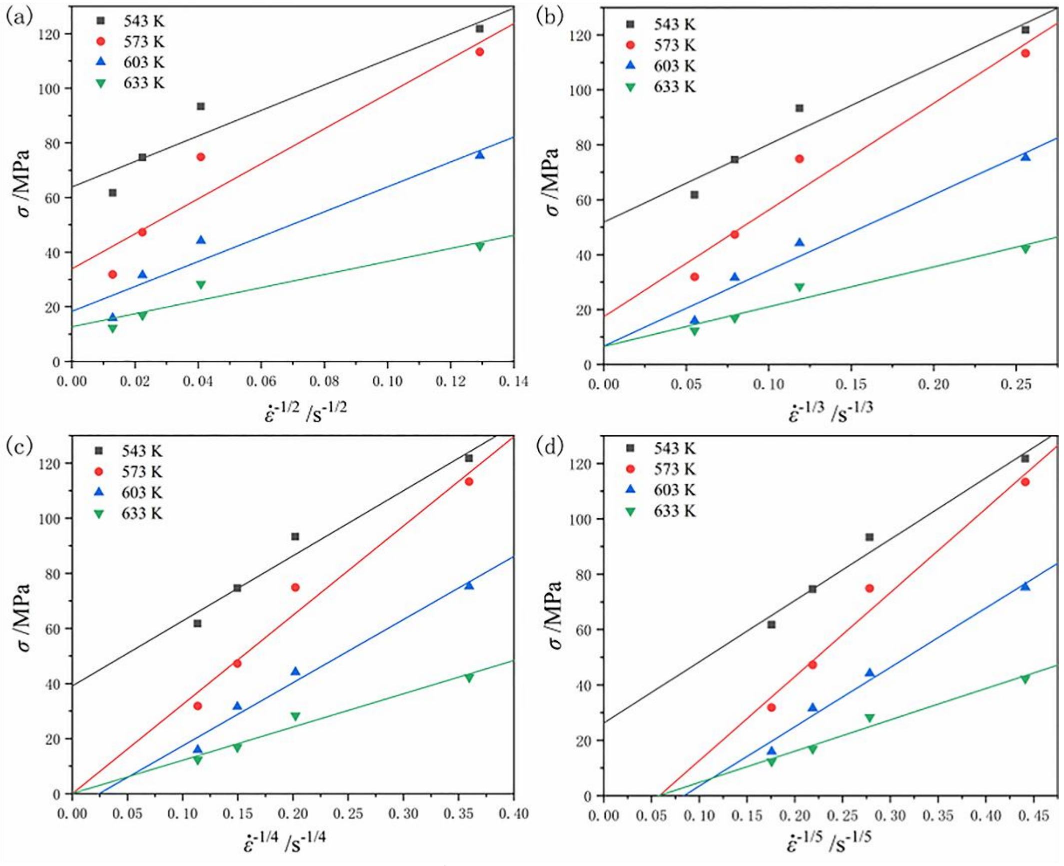

Fig. 16. Fitting curves of σ versus $\dot{\varepsilon}^{1/n}$ of LAZY3720 alloy: (a)n=2; (b)n=3; (c)n=4; (d)n=5.

The correlation coefficients corresponding to n value of 2, 3, 4, and 5 are 0.65, 0.9758, 0.9843, and 0.9886, respectively. As shown in Fig. 16, the threshold stress is positive when n values are 2 and 3, but the threshold stress is negative when n values are 4 and 5. Thus, n=4 and 5 are ruled out or excluded. Thus, n=3 is the best stress exponent or true stress exponent.

(2) Activation energy for deformation Q

True activation energy for deformation at constant strain rate is given by the following relation based on Eq. (15):

$$Q = R\frac{\partial[\ln(\sigma^n G^{1-n} T^{-1} d^{-p})]}{\partial(T^{-1})}\bigg|_{\dot{\varepsilon}} \qquad (16)$$

Since dislocation creep is predominant in the present alloy, p is equal to zero [42].

Fig. 17 shows the fitting curves of $\ln(\sigma^n G^{1-n} T^{-1}) - 1/T$ at different strain rates.

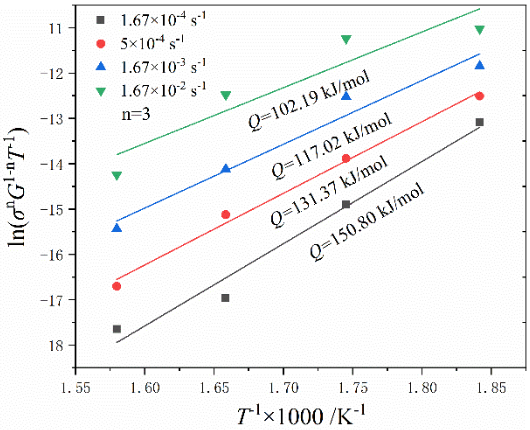

Fig. 17. Fitting curves of $\ln(\sigma^n G^{1-n} T^{-1}) - 1/T$ at different strain rates.

The activation energy for high temperature deformation of LAZY3720 alloy is in the range of 102.19-150.8 kJ/mol.

（3）Normalized curve

Eq. (15) is converted into the following form by taking logarithm:

$$\ln\left(\frac{\dot{\varepsilon}kT}{DGb}\right) = \ln A + n\ln\frac{\sigma-\sigma_0}{G} \qquad (17)$$

where $D = D_0\exp[-Q/RT]$，D_0=1×10^{-4} m^2 s^{-1} [43] ,Q is the average activation energy for deformation, Q=125.343 kJ/mol.

Fig. 18 shows the fitting curve of $\ln(\dot{\varepsilon}kT/DGb) - \ln[(\sigma-\sigma_0)/G]$. The slope of the linear fitting line is 2.5 (≈3),. The intercept of the fitting line is $\ln A$ (= -3.91). Thus, A =0.02. Correlation coefficient, R, is 0.84647, and absolute error is less than 16%.

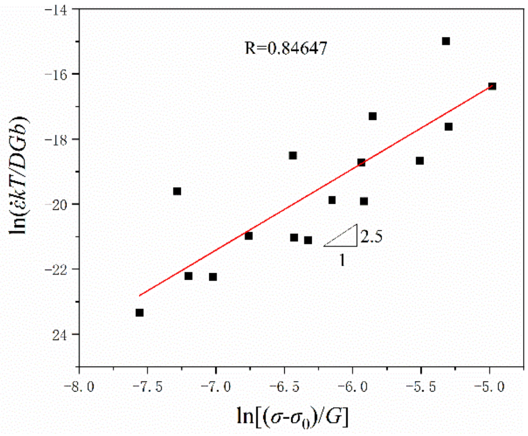

Fig. 18. Fitting curve of $\ln(\dot{\varepsilon}kT/DGb) - \ln[(\sigma-\sigma_0)/G]$.

Hence, the power-law constitutive equation of LAZY3720 alloy is obtained:

$$\dot{\varepsilon} = 2 \times 10^{-2} D_0 \frac{Gb}{KT} \left(\frac{\sigma - \sigma_0}{G}\right)^3 \exp\left(\frac{-125343}{RT}\right) \qquad (18)$$

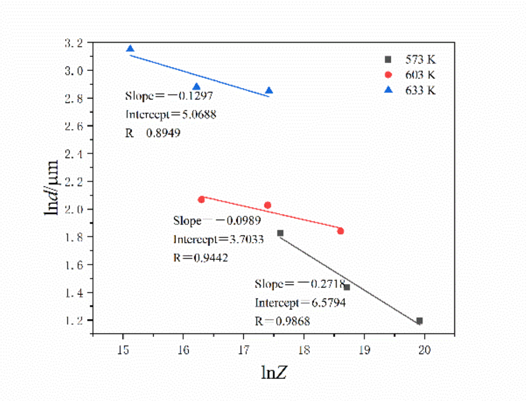

Fig. 19. The plot of ln*d* as a function of ln*Z*.

Finally, the relationship between average grain size and Zener-Hollomon parameter (Z parameter) needs to be established. Z parameter is given by [44]

$$Z = \dot{\varepsilon} \exp\left[\left(\frac{Q}{RT}\right]\right. \qquad (19)$$

Presuming that $d = aZ^{n'}$, where a and n' are constants. Taking logarithm on both sides, one gets

$$lnd = \ln a + n' \ln Z \qquad (20)$$

Fig. 19 shows the plot of ln*d* against ln*Z*. a=166.863, and n'=-0.16679. Hence, the relationship of *d* and *Z* can be obtained.

$$d = 166.863 Z^{-0.16679} \qquad (21)$$

IV. Discussion

4.1. Analysis of microstructural evolution and mechanical properties at tensile temperatures

As depicted in Sections 3.2 and 3.3, the temperature and strain rate have a significant influence on the flow stress level. The flow stress level decreases with increasing the temperature and/or decreasing the strain rate. The reason is that due to thermal activation process at elevated temperature, atomic diffusion accelerates, and dislocation density decreases. As a result, the flow stress level decreases with increasing the temperature and/or decreasing the strain rate. As shown in Figs. 5, 6, 7 and 8, DRX occurs to a great extent in the microstructures, and flow softening occurs in most cases. As such, the flow stress curve exhibits a slow decreasing stress curve after the peak stress, i.e., flow softening phenomenon. That is because Mg has a lower stacking fault energy than Al, DRX instead of dynamic recovery (DRV) easily occurs in the present ultralight alloy. Since serrated grain boundary does not appear in the microstructures, geometrical DRX is excluded. As shown in Fig. 6 (c) and Fig. 7(a)(b), some of extremely small grains are around the big grains, which reveals the nucleation and growth in some sites. This demonstrates the occurrence of discontinuous DRX. Furthermore, according to Mohri et al. work [45] and superplasticity theory, hot tensile process involves the transformation of low angle grain boundary to high angle grain boundary due to the reduction of grain size from coarse grain to fine grain with increasing the true strain. This transformation indicates the occurrence of continuous DRX [45, 46]. The cause of occurrence of continuous DRX is as follows: under applied tensile stress or strain at elevated temperature, subgrains with low angle grain boundary in coarse grain rotate and undergo the increase in misorientation angle by absorption of dislocations and turn into equiaxed grains with high angle grain boundary. Grain refinement due to continuous DRX results in flow softening. According to above-mentioned analysis, we come to the conclusion that discontinuous DRX and continuous DRX occur in this alloy during the hot tensile process. However, as shown in Figs. 7(c)(d) and 8(d), the flow stress increases with increasing the strain at a temperature of 633 K and strain rates of 5×10^{-4} -1.67×10^{-4} s^{-1}, indicative of the occurrence of grain coarsening and flow hardening phenomenon. Under applied stress or imposed strain at 633 K, thermal activation accelerates atomic diffusion and promotes grain boundary migration. Grain boundary migration induces dynamic grain coarsening, called strain-enhanced grain coarsening. The flow hardening phenomenon has been found in superplastic CoCrFeNiMn high entropy alloy [47] and superplastic ZK30 magnesium alloy [48]. Due to grain coarsening, the number of dislocations in Eqs. (11) and (13) increases, stress exponent increases, and strain hardening appears at the flow stress curves. In a word, dynamic grain coarsening results in strain hardening. The increase in stress exponent at elevated temperature is a recent discovery and advancement in some of alloys subjected to high temperature deformation. An inconsistency exists between the microstructures in Fig. 7(a)(b) and the flow stress curves in Fig. 8(d) at 633 K and 1.67×10^{-2} -1.67×10^{-3} s^{-1} and remains to be investigated in the future.

4.2. Comparative analysis of two established constitutive equations

mZA constitutive equation and power-law constitutive equation possess different characteristics. mZA constitutive equation has its phenomenological nature while power-law constitutive equation has its physical nature. As shown in Sections 3.4.1 and 3.4.2, the result demonstrates that the established mZA model is relevant to temperature, strain rate, and strain and suitable for describing the hot forming process at higher temperatures of 573-633 K and strain rates of 1.67×10^{-2} and 1.67×10^{-4} s^{-1}, whereas the established power-law constitutive equation is relevant to temperature and strain rate and appropriate for tensile process of superplasticity and creep.

On one hand, if mZA constitutive equation were embedded into the control system of forging press and rolling mill, the control panel would display much useful information such as deformation temperature, strain rate or velocity, strain, stress, grain size, dislocation density, and the number of dislocations inside a grain. As a result, the macroscopic deformation conditions and microscopic parameters can be monitored. In this way can the manufacturer monitor and manage the technological process. Thus, mZA constitutive modeling has both scientific value and practical meaning.

On the other hand, power-law constitutive modeling involves characteristic values such as n, p, and Q and helps to deepen the understanding of the high temperature deformation mechanism. As shown in Section 3.4, in consideration of the stress exponent, 2.5 (≈3), dislocation density, 1.08×10^{14} m^{-2}, and a number of dislocations, 27, it is evidenced that dislocation glide creep is the dominant deformation mechanism of this alloy at a deformation temperature of 573 K and a strain rate of 1.67×10^{-4} s^{-1}. Moreover, the experimental activation energy for deformation is in the range of 102.19~150.8 kJ/mol at strain rates of 1.67×10^{-2} ~1.67×10^{-4} s^{-1}. According to reference [49], the theoretical activation energy of Mg grain boundary diffusion is 92 kJ/mol while the theoretical activation energy of Mg lattice diffusion is 135 kJ/mol. The experimental activation energy for deformation of 102.19 kJ/mol at a strain rate of 1.67×10^{-2} s^{-1} is slightly higher than the theoretical activation energy of Mg grain boundary diffusion of 92 kJ/mol. The experimental activation energy for deformation of 150.8 kJ/mol at a strain rate of 1.67×10^{-4} s^{-1} is more than the theoretical activation energy of Mg lattice diffusion of 135 kJ/mol. This is because the second phase obstructs the movement of dislocations, raises the energy barrier, and increases the deformation activation energy. This result reveals that the experimental diffusion process experiences a transition from grain boundary diffusion to lattice diffusion at strain rates of 1.67×10^{-2} ~1.67×10^{-4} s^{-1}. In view of the abovementioned discussions, it is concluded that the rate-controlling mechanism of this alloy at 573 K and 1.67×10^{-4} s^{-1} is dislocation glide creep controlled by lattice diffusion.

4.3. Distinguishing feature of dislocations in complex multicomponent LAZY3720 alloy

The number of dislocations inside a grain has a significant influence on the deformation mechanism in this alloy. As shown in Figs. 2(b) and 5(d), since the grain size undergoes a transition from 16.5 ± 1.3 μm coarse grain in the annealed state to 6.2 ± 1.2 μm fine grain in the deformed state, this indicates the occurrence of DRX. Meanwhile, the calculated number of dislocations inside a grain decreases from 135 to 27 at a temperature of 573 K and a strain rate of 1.67×10^{-4} s^{-1}. A large number of dislocations inside a grain obstruct the occurrence of GBS. This is quite different from the deduction in β-Li phase based coarse grained Mg-Li-Al alloy in reference [50], probably because the present alloy is a α-Mg phase based coarse grained alloy in its initial state, and the interaction between dislocations and solutes Li, Al, and Zn may hinder the appearance of GBS even if the occurrence of DRX grain refinement during the tensile process. So many dislocations, number of dislocations of 27-135, exist inside a grain and promote intragranular dislocation glide under applied uniaxial tensile stress. Although the grain size in the gauge section is in a fine grain scale, so many dislocations obstruct the occurrence of the GBS because typical superplastic alloys usually contain only a few dislocations, say, 1-12, in reference [51] rather than dozens of dislocations in the present alloy. This finding means that too many dislocations inside a fine grain formed by DRX favor intragranular dislocation glide and disfavor GBS, which is our contribution to superplasticity and creep theory. That is a distinguishing feature of complex system LAZY3720 alloy compared to simple system Mg-Li alloy. In addition, the maximum elongation of 310% is below 400% which is a typical value of classical superplasticity [16]. This elongation indicates that the high temperature deformation nature belongs to superplasticity-like behavior or quasi-superplasticity with an elongation of 200-300%. Also, aforementioned n-value is adjacent to 3, and the strain rate sensitivity exponent m-value is adjacent to 0.33 (m=1/n). Thus, the role of dislocation glide is the predominant. Thus, dislocation glide creep mechanism seems to be reasonable under this condition.

Furthermore, the rationality of the number of dislocations inside a grain and dislocation density (27 and 1.08×10^{14} m^{-2} m^{-2}) at 573 K and 1.67×10^{-4} s^{-1} is analyzed. According to our previous report on Al−1.88Mg−0.18Sc−0.084Er alloy during uniaxial hot compression at 773 K and 10^{-3} s^{-1} [52], the estimation of the number of dislocations and dislocation density (18 and 2.99×10^{13} m^{-2}) and experimental evidence (21 and 1.16×10^{13} m^{-2}) demonstrated that corresponding dislocation variable models were validated and convincing. That is to say, Eqs. (11, 13) and (10, 12) are convincing. As such, the estimated number of dislocations and dislocation density in the present alloy are convincing.

4.4. Comparison of the present results with current research about high temperature deformation

Recently, Xiao et al. [53] proposed a dislocation density-based constitutive equation in hot compressed Ti-55111 based alloy based on Kocks' work. In Section 3.4.1, mZA constitutive equation considering dislocation density and the number of dislocations are based on our previous work on dislocation variables. The common characteristic is that both reports reflect the relationship between dislocation density and thermal deformation condition (deformation temperature, strain rate, and strain). Recently, Kim et al. [54] connected Prasad's hot processing map based on dynamic material model to Ruano-Sherby's deformation mechanism map based on creep constitutive equation. In Section 3.4.1, the embedment of mZA constitutive equation into our work on dislocation variables can realize the connection between the number of dislocations and thermal deformation condition, which is a further development of the deformation mechanism map containing the number of dislocations in microduplex magnesium-lithium alloy [55] and further development of the establishment of our Arrhenius constitutive equations incorporating dislocation variables in hot compressive Al-1.88Mg-0.18Sc-0.084Er alloy [52] and hot tensile Mg-4.4Li-2.5Zn-0.46Al-0.74Y alloy [56]. In terms of this analysis, it is found that abovementioned high temperature deformation study is bridging the gap between hot deformation process and high temperature superplasticity and creep. Ashby's prophecy on internal state variables in reference [57] has been realized in references [52-56] and the present work.

4.5. Novelty statement and important findings in this work

The following innovations and important findings have been reported as per above-mentioned experimental results and theoretical analysis. Firstly, a novel α-Mg based multicomponent Mg-2.65Li-7.05Al-2.08Zn-0.15Y alloy with an emphasis on high Al content (7.05%) has been successfully fabricated by decreasing-temperature multidirectional forging and hot rolling. The ultimate tensile strength, 0.2% proof stress, and elongation of 295 MPa, 200 MPa, and 17.79%, respectively, were obtained at room temperature in this alloy. Secondly, the maximum quasi-superplasticity of 310% was demonstrated in this alloy with an average grain size of 13.94 ± 1.0 μm at a temperature of 573 K and a strain rate of 1.67×10^{-4} s^{-1}. Thirdly, flow stress curves and microstructural examination showed that discontinuous DRX and continuous DRX occurred in this alloy at elevated temperatures and different strain rates in most cases, but the flow hardening phenomenon resulting from the occurrence of dynamic grain coarsening was discovered in a few cases. Fourthly, the result demonstrated that the established mZA model was suitable for describing the hot forming process at higher temperatures of 573-633 K and strain rates of 1.67×10^{-2} and 1.67×10^{-4} s^{-1} in this alloy. The established mZA constitutive model was incorporated into dislocation models to realize the estimation of the dislocation density and number of dislocations inside a grain under specific conditions. It was discovered that dozens of dislocations inside a fine grain formed by DRX favored intragranular dislocation glide and disfavored grain boundary sliding, which is our contribution to superplasticity and creep theory. Fifthly, it was found that in this alloy (average grain size of 13.94 ± 1.0 μm at 573 K and 1.67×10^{-4} s^{-1}, the stress exponent was 3, and the experimental activation energy for deformation was 150.8 kJ/mol; the dislocation density was 1.08×10^{14} m^{-2}, and the number of dislocations inside a grain was 27. These results confirmed that the rate-controlling deformation mechanism of this alloy under this condition is dislocation viscous glide creep controlled by lattice diffusion.

V. Conclusions

(1) A novel multicomponent Mg-2.65Li-7.05Al-2.08Zn-0.15Y alloy has been successfully fabricated by decreasing-temperature multidirectional forging and hot rolling. The optical microstructural examination revealed that the average grain size of the processed alloy plate was 13.94 ± 1.0 μm while the average grain size of as-annealed alloy was 16.5 ± 1.3 μm. The ultimate tensile strength, 0.2% proof stress, and elongation of 295 MPa, 200 MPa, and 17.79%, respectively, were obtained at room temperature. The maximum superplasticity of 310% was demonstrated in this alloy at a temperature of 573 K and a strain rate of 1.67×10^{-4} s^{-1}.

(2) Flow stress curves and microstructural examination showed that discontinuous dynamic recrystallization and continuous dynamic recrystallization occurred in this alloy at elevated temperatures and different strain rates in most cases, but the flow hardening phenomenon was discovered that the flow stress increases with increasing the strain at a temperature of 633 K and strain rates of 5×10^{-4} -1.67×10^{-4} s^{-1}, resulting from the occurrence of dynamic grain coarsening.

(3) The result demonstrated that the established mZA model was suitable for describing the hot forming process at higher temperatures of 573-633 K and strain rates of 1.67×10^{-2} and 1.67×10^{-4} s^{-1} in this alloy. The

established mZA constitutive model was incorporated into dislocation models to realize the estimation of the dislocation density and number of dislocations inside a grain under specific conditions. It was discovered that dozens of dislocations inside a fine grain formed by dynamic recrystallization favored intragranular dislocation glide and disfavored grain boundary sliding. A power-law constitutive equation was established, and the relationship between average grain size and Zener-Hollomon parameter was established in this alloy.

(4) It was found that at 573 K and 1.67×10^{-4} s^{-1}, the stress exponent was 3, and the experimental activation energy for deformation was 150.8 kJ/mol; the dislocation density was 1.08×10^{14} m^{-2}, and the number of dislocations inside a grain was 27. These results confirmed that the predominant deformation mechanism of this alloy under this condition is dislocation viscous glide creep controlled by lattice diffusion.

Acknowledgments

This work is supported financially by the National Natural Science Foundation of China [No. 51334006].

References

[1]. Y. Wang, Y. Liao, R.Z. Wu, N. Turakhodjaev, H. T. Chen, J. H. Zhang, M.L. Zhang, S. Mardonakulov, Microstructure and mechanical properties of ultra-lightweight Mg-Li-Al/Al-Li composite produced by accumulative roll bonding at ambient temperature, Mater. Sci. Eng. A 787 (2020) 139494, https://doi.org/10.1016/j.msea.2020.139494.

[2]. T. Mineta, K. Kumatani, H. Adachi, H. Sato, Dependence of the mechanical properties and microstructure of ultralight magnesium-lithium-aluminum alloy on heat treatment conditions, Materialwiss. Werkstofftech. 52(2021**)** 339–345, https://doi.org/10.1002/mawe.202000250.

[3]. Q. Ji, Y. Wang, R.Z. Wu, Z. Wei, X.C. Ma, J.H. Zhang, L.G. Hou, M.L. Zhang, High specific strength Mg-Li-Zn-Er alloy processed by multi deformation processes, Mater. Charact. 160 (2020) 110135, https://doi.org/10.1016/j.matchar.2020.110135.

[4]. F. Guo , L.Liu, Y.L. Ma, L.Y. Jiang, D.F. Zhang, F.S. Pan, Mechanism of phase refinement and its effect on mechanical properties of a severely deformed dual-phase Mg–Li alloy during annealing, Mater. Sci. Eng. A 772 (2020) 138792, https://doi.org/10.1016/j.msea.2019.138792.

[5]. G. Liu, Z.D. Ma, G.B. Wei, T.C. Xu. Zhang, Y. Yang, W.D. Xie, X.D. Peng, Microstructure, tensile properties and corrosion behavior of friction stir processed Mg-9Li-1Zn alloy, J. Mater. Proc. Technol. 267 (2019) 393-402, https://doi.org/10.1016/j.jmatprotec.2018.12.026.

[6]. X.L.Liang, X.Peng, H.Ji, W.C. Liu, G.H. Wu, W. J. Ding, Microstructure and mechanical properties of as-cast and solid solution treated Mg−8Li−*x*Al−*y*Zn alloys, Trans. Nonferrous Met. Soc. China 31 (2021) 925-938, https://doi.org/10.1016/S1003-6326(21)65550-4.

[7]. Z.J. Yu, L.L. Liu, A. Mansoor, K. Liu, S. B. Li, W.B. Du, Microstructures and mechanical properties of as-extruded Mg-8Gd-2Y-1Zn-6Li alloy, J. Alloys Compd. 864 (2021) 158826, https://doi.org.10.1016/j/jallcom.2021.158826.

[8]. F. Zhong, Y. Wang, R.Z. Wu, J.H. Zhang, L.G. Hou, M.L. Zhang, Effect of rolling temperature on deformation behavior and mechanical properties of Mg-8Li-01Al-0.6Y-0.6Ce alloy, J. Alloys Compd. 831 (2020) 154765, https://doi.org/10.1016/j.jallcom.2020.154765.

[9]. B. Shao, S.F. Wu, D.B. Shan, B. Guo, Y.Y. Zong, The effect of thermal cycling process between high and low temperatures on the microstructure and properties of Mg-10Li-3Al-3Zn-0.25Si alloy, Mater. Lett. 254 (2019) 167-170. https://doi.org/10.1016/j.matlet.2019.07.057.

[10]. X. Peng, S.H. Xu, D.H. Ding, G.L. Liao, G.H. Wu, W.C. Liu, W.J. Ding, Microstructural evolution, mechanical properties and corrosion behavior of as-cast Mg-5Li-3Al-2Zn alloy with different Sn and Y addition, J. Mater. Sci. Technol. 72 (2021) 16-22, https://doi.org/10.1016/j.jmst.2020.07.029.

[11]. J. Zhao, B. Jiang, A.T. Tang, Y.F. Chai, B. Liu, H.R. Sheng, T.H. Yang, G.S. Huang, D.F. Zhang, F.S. Pan, Deformation behavior and texture evolution in an extruded Mg-Li sheet with non-basal texture during tensile deformation, Mater. Charact. 159 (2020) 110041, https://doi.org/10.1016/j.matchar.2019.110041.

[12]. T. Mineta, K. Hasegawa, H. Sato, High strength and plastic deformability of Mg-Li-Al alloy with dual BCC phase produced by a combination of heat treatment and multi-directional forging in channel die, Mater. Sci. Eng. A 773 (2020) 138867. https://doi.org/10.1016/j.msea.2019.138867.

[13]. M. Kobayashi, Y. Yoden, T. Aoba, H. Miura, Microstructure and mechanical properties of multi-directionally-forged AZ80-F magnesium alloys at warm temperatures, J. Japan Inst. Met. Mater. 84(6) (2020) 190-199, https://doi.org/10.2320/jinstmet.J2019043.

[14]. F.R. Cao, G.Q. Xue, G.M. Xu, Superplasticity of a dual-phase-dominated Mg-Li-Al-Zn-Sr alloy processed by multidirectional forging and rolling, Mater. Sci. Eng. A 704 (2017) 360-374, https://doi.org/10.1016/j.msea.2017.08.037.

[15]. F.R. Cao, J. Zhang, X. Ding, G.Q. Xue, S.Y. Liu, C.F. Sun, R.K. Su, X.M. Teng, Mechanical properties and microstructural evolution in a superlight Mg-6.4Li-3.6Zn-0.37Al-0.36Y alloy processed by multidirectional forging and rolling, Mater. Sci. Eng. A 760 (2019) 377-393, https://doi.org/10.1016/j.msea.2019.06.009.

[16]. T.G. Langdon, Seventy-five years of superplasticity: historic developments and new opportunities, J. Mater. Sci. 44(2009) 5998-6010,https://doi.org/10.1007/s10853-009-3780-5.

[17]. H.P. Yang, X. Zhang, P. Chen, M.W. Fu, G.C. Wang, S. To, Investigation on the enhanced maximum strain rate sensitivity (m) superplasticity of Mg-9Li-1Al alloy by a two-step deformation method, Mater. Sci. Eng. A 764(2019) 138219, https://doi.org/10.1016/j.msea.2019.138219.

[18]. T.L. Zhang, T. Tokunaga, M. Ohno, R.Z. Wu, M.L. Zhang, K. Matsuura, Low temperature superplasticity of a dual-phase Mg-Li-Zn alloy processed by a multi-mode deformation process, Mater. Sci. Eng. A 737(2018) 61-68, https://doi.org/10.1016/j.msea.2018.08.081.

[19]. A. Mehrabi, R. Mahmudi, H. Miura, Superplasticity in a multi-directionally forged Mg–Li–Zn alloy, Mater. Sci. Eng. A 765(2019) 138274, https://doi.org/10.1016/j.msea.2019.138274.

[20]. M. R. Zhou , Y. Morisada, H. Fujii, J.Y. Wang, Pronounced low-temperature superplasticity of friction stir processed Mg–9Li–1Zn alloy, Mater. Sci. Eng. A 780(2020) 139071, https://doi.org/10.1016/j.msea.2020.139071.

[21]. D.X. Chen, J. Kong, Z.Z. Gui, W. Li, Y. Long, Z.X. Kang, High-temperature superplastic behavior and ECAP deformation mechanism of two-phase Mg-Li alloy, Mater. Lett. 301(2021) 130358, https://doi.org/10.1016/j.matlet.2021.130358.

[22]. Y.C. Lin, X.M. Chen, A critical review of experimental results and constitutive descriptions for metals and alloys in hot working, Mater. Des. 32 (2011) 1733–1759, https://doi.org/10.1016/j.matdes.2010.11.048.

[23]. N. Ansari, B. Tran, W. J. Poole, S. S. Singh, H. Krishnaswamy, J. Jain, High temperature deformation behavior of Mg-5wt.%Y binary alloy: Constitutive analysis and processing maps, Mater. Sci. Eng. A 777 (2020) 139051, https://doi.org/10.1016/j.msea.2020.139051.

[24]. A. Sheikhani, R. Roumina, R. Mahmudi, Hot deformation behavior of an extruded AZ31 alloy doped with rare earth elements, J. Alloys Compd. 852 (2021) 156961, https://doi.org/10.1016/j.jallcom.2020.156961.

[25]. J.C. Long , Q.X. Xia , G.F. Xiao , Y. Qin , S. Yuan, Flow characterization of magnesium alloy ZK61 during hot deformation with improved constitutive equations and using activation energy maps, Int. J. Mech. Sci. 191 (2021) 106069, https://doi.org/10.1016/j.ijmecsci.2020.106069.

[26]. W.R Tang, S.M. Liu, Z. Liu, S. Kang, P.L. Mao, H. Guo, High strain rate compression deformation mechanism and constitutive equation of fine grained Mg–7Gd–5Y–1.2Nd–0.5Zr alloy at different temperatures, Mater. Sci. Eng. A 780 (2020) 139208, https://doi.org/10.1016/j.msea.2020.139208.

[27]. C. Y. Seif , I. S. Hage, R. F. Hamade, Extracting HCP Zerilli-Armstrong material parameters for magnesium alloy AZ31B from orthogonal cutting tests, J. Mater. Proc. Technol. 290 (2021) 116982, https://doi.org/10.1016/j.jmatprotec.2020.116982.

[28]. B. Mishra, A. Mukhopadhyay, K. S. Kumar, D. V. Kumar, K. N. Jonnalagadda, M.J.N.V. Prasad, Effect of test temperature on flow behavior and strain hardening of magnesium under high strain rate deformation conditions, Mater. Sci. Eng. A 770 (2020) 138546, https://doi.org/10.1016/j.msea.2019.138546.

[29]. M. Shalbafi, R .Roumina, R. Mahmudi, Hot deformation of the extruded Mg-10Li-1Zn alloy: Constitutive analysis and processing maps, J. Alloys Compd. 696 (2017) 1269-1277, https://doi.org/10.1016/j.jallcom.2016.12.087.

[30]. G. Liu, W. Xie, A. Hadadzadeh, G.B. Wei, Z.D. Ma,J.W. Liu,Y.Yang, W.D. Xie, X.D. Peng, M. Wells, Hot deformation behavior and processing map of a superlight dual-phase Mg-Li alloy, J. Alloys Compd. 766 (2018) 460-469, https://doi.org/10.1016/j.jallcom.2018.07.024.

[31]. T. C. Xu, X. D. Peng, J .Qin, Y.F.Chen, Y.Yang, G.B.Wei , Dynamic recrystallization behavior of Mg-Li-Al-Nd duplex alloy during hot compression, J. Alloys Compd. 639 (2015) 79-88, https://doi.org/10.1016/j.jallcom.2015.03.144.

[32]. Y. Li, Y. J. Guan, J. Q. Zhai, J. Lin, Hot deformation behavior of LA43M Mg-Li alloy via hot compression tests, J. Mater. Eng. Perform. 28 (2019) 7768-7781, https://doi.org/10.1007/s11665-019-04500-6.

[33]. R. Tsukane, H. Tamai, M. Nogawa, Y. Harada, K. Matsuzaki, T. Nagoshi, Hot compression behavior of Mg-14Li-6Al-1Ca alloy, Mater. Trans. 61 (2020) 2101- 2106, https://doi.org/10.2320/matertrans.MT-M2020157.

[34]. X.Q. Li , Q.C. Le, D.D. Li, P. Wang, P.P. Jin, C.L. Cheng, X.R. Chen, L. Ren, Hot tensile deformation behavior of extruded LAZ532 alloy with heterostructure, Mater. Sci. Eng. A 801 (2021) 140412, https://doi.org/10.1016/j.msea.2020.140412.

[35]. F.R. Cao, F. Xia, H.L. Hou , H. Ding, Z.Q. Li, Effects of high-density pulse current on mechanical properties and microstructure in a rolled Mg-9.3Li-1.79Al-1.61Zn alloy, Mater. Sci. Eng. A 637(2015) 89-97, https://doi.org/10.1016/j.msea.2015.03.127.

[36]. H.Y. Li , Y.H. Li , X.F. Wang , J.J. Liu, Y. Wu, A comparative study on modified Johnson Cook, modified Zerilli–Armstrong and Arrhenius-type constitutive models to predict the hot deformation behavior in 28CrMnMoV steel, Mater. Des. 49 (2013) 493-501, https://doi.org/10.1016/j.matdes.2012.12.083.

[37]. F.R. Cao, F. Xia, G.Q. Xue, Hot tensile deformation behavior and microstructural evolution of a Mg-9.3Li-1.79Al-1.61Zn alloy, Mater. Des. 92 (2016) 44-57, https://doi.org/10.1016/j.matdes.2015.12.008.

[38]. M. Kawasaki, K. Kubota, K. Higashi, T.G. Langdon, Flow and cavitation in a quasi-superplastic two-phase magnesium-lithium alloy, Mater. Sci. Eng. A 429 (2006) 334-340, https://doi.org/10.1016/j.msea.2006.05.043.

[39]. T. G. Langdon, F. A. Mohamed, A new type of deformation mechanism map for high-temperature creep, Mater. Sci. Eng. 32 (1978) 103-112, https://doi.org/10.1016/0025-5416(78)90029-0.

[40]. F. R. Cao, B.J. Zhou, B. Yin, G.Q. Xue, X.T. Zhu, G, M. Xu, Modeling of deformation energy at elevated temperatures and its application in Mg-Li-Al-Y alloy, Trans. Nonferrous Met. Soc. China 27 (2017) 2434-2442, https://doi.org/10.1016/S1003-6326(17)60270-X.

[41]. T.G. Langdon, A unified approach to grain boundary sliding in creep and superplasticity, Acta Metall. Mater. 42 (1994) 2437–2443, https://doi.org/10.1016/0956-7151(94)90322-0.

[42]. M.E. Kassner, M.T. Perez-Prado, Five-power-law creep in single phase metals and alloys, Prog. Mater. Sci. 45 (2000) 1-102, https://doi.org/10.1016/S0079-6425(99)00006-7.

[43].]E.M. Taleff, O.A. Ruano, O.D. Sherby, Superplastic behavior of a fine-grained Mg-9Li materials at low homologous temperature, J. Mater. Res. 7 (1992) 2131-2135, https://doi.org/10.1557/jmr.1992.2131.

[44]. C. Zener, J. H. Hollomon, Effect of strain rate upon plastic flow of steel, J Appl. Phys. 15 (1944) 22-32, https://doi.org/10.1063/1.1707363.

[45]. T. Mohri, M. Mabuchi, M. Nakamura, T. Asahina, H. Iwasaki, T. Aizawa, K. Higashi, Microstructural evolution and superplasticity of rolled Mg-9Al-1Zn, Mater. Sci. Eng. A 290 (2000) 139–144, https://doi.org/10.1016/S0921-5093(00)00959-X.

[46]. T. Sakai, A. Belyakov, R. Kaibyshev, H. Miura, J. J. Jonas, Dynamic and post dynamic recrystallization under hot, cold and severe plastic deformation conditions, Prog. Mater. Sci. 60 (2014) 130–207, https://doi.org/10.1016/j.pmatsci.2013.09.002.

[47]. H. Shahmir, J.Y. He, Z.P. Lu, M. Kawasaki, T. G. Langdon, Evidence for superplasticity in a CoCrFeNiMn high-entropy alloy processed by high-pressure torsion, Mater. Sci. Eng. A 685 (2017) 342-348, https://doi.org/10.1016/j.msea.2017.01.016.

[48]. M. Álvarez-Leal, A. Orozco-Caballero, F. Carreno, O. A. Ruano, Superplasticity in a commercially extruded ZK30 magnesium alloy, Mater. Sci. Eng. A 710 (2018) 240-244,https://doi.org/10.1016/j.msea.2017.10.093.

[49]. H.J. Frost, M.F. Ashby, Deformation Mechanism Maps, Pergamon Press, Oxford, UK, 1982, p. 21.

[50]. M. Kawasaki, R. B. Figueiredo, T.G. Langdon, The requirements for superplasticity with an emphasis on magnesium alloys, Adv. Eng. Mater. 18 (2016) 127-131, https://doi.org/10.1002/adem.201500068.

[51]. F.R. Cao, Incorporating dislocation variables into Mohamed's and Kawasaki-Langdon's deformation mechanism maps containing superplasticity mechanism regimes, Mater. Sci. Eng. A 643 (2015) 169-174, https://doi.org/10.1016/j.msea.2015.07.042.

[52]. F.R. Cao, B. Yin, S.Y. Liu, L. Shi, S.C. Wang, J.L. Wen, Microstructural evolution, flow stress and constitutive modeling of a novel Al-1.88Mg-0.18Sc-0.084Er alloy during hot compression, Trans. Nonferrous Met. Soc. China 31 (2021) 53-73, https://doi.org/10.1016/S1003-6326(20)65478-4.

[53]. Y.W. Xiao, Y.C. Lin, Y.Q. Jiang, X.Y. Zhang, G.D. Pang, D. Wang , K.C. Zhou, A dislocation density-based model and processing maps of Ti-55511 alloy with bimodal microstructures during hot compression in α+β region, Mater. Sci. Eng. A 790 (2020) 139692, https://doi.org/10.1016/j.msea.2020.139692.

[54]. W.J. Kim, H.T. Jeong, Construction of processing maps combined with deformation mechanism maps using creep deformation equations, J. Mater. Res. Technol. 9 (2020) 13434–13449, https://doi.org/10.1016/j.jmrt.2020.09.023.

[55]. F. R. Cao, H. Ding, Y. L. Li, G. Zhou, J. Z. Cui, Superplasticity, dynamic grain growth and deformation mechanism in ultralight two-phase magnesium-lithium alloys, Mater. Sci. Eng. A 527 (2010) 2335-2341, https://doi.org/10.1016/j.msea.2009.12.029.

[56]. F.R. Cao, X. Ding, C. Xiang, H.H. Shang, Flow stress, microstructural evolution and constitutive analysis during high-temperature deformation in an Mg-4.4Li-2.5Zn-0.46Al-0.74Y Alloy, Acta Metall. Sin. 57 (2021) 860-870, https://doi.org/10.11900/0412.1961.2020.00306.

[57]. M.F. Ashby, Physical modelling of materials problems, Mater. Sci. Technol. 8 (1992) 102-111, https://doi.org/10.1179/mst.1992.8.2.102.